PAPER

Anisotropic swelling of thin gel sheets

Paola Nardinocchi,*[a] Matteo Pezzulla[a] and Luciano Teresi[b]

We describe the anisotropic swelling within the Flory–Rehner thermodynamic model through an extension of the elastic component of the free-energy, which takes into account the oriented hampering of the swelling-induced deformations due to the presence of stiffer fibers. We also characterize the homogeneous free-swelling solutions of the corresponding anisotropic stress-diffusion problem, and discuss an asymptotic approximation of the key equations, which allows us to explicitly derive the anisotropic solution of the problem. We propose a proof-of-concept of our model, realizing thin bilayered gel sheets with layers having different anisotropic structures. In particular, for seedpod-like sheets, we observe and quantitatively measure the helicoid *versus* ribbon transition determined by the aspect ratio of the composite sheet.

1. Introduction

Soft active materials have been largely employed to realize actuators where deformations and displacements are triggered by a wide range of external stimuli such as electric field, pH, temperature, and solvent absorption.[1–4] The effectiveness of these actuators critically depends on the capability of achieving prescribed changes in their shape and size. In particular, in gel-based actuators, the shape and the size of the structures are related to the spatial distribution of the solvent inside the gel and to the magnitude of the solvent uptake. Currently, several approaches to the shape control of swellable materials are being pursued, which involve materials in the form of thin non-homogeneous sheets realized through a controlled assembly of gels which separately admit a different swelling degree.[5–8] It has been shown that these non-homogeneous structures can deliver homogeneous free-swelling processes, which can be isotropic[5] as well as anisotropic,[6] depending on the architecture of the assembly. Photo-patterned multi-strip thin films belong to this last class: they undergo anisotropic expansion under free-swelling conditions, when the size of the strips goes below a critical threshold. The films act as a composite material containing stiffer low-swelling strips and softer high-swelling strips; swelling-induced deformations are smaller in the direction parallel to the interfaces than those along the orthogonal direction.[6]

Starting from these observations, we describe the anisotropic swelling within the Flory–Rehner thermodynamic model through an extension of the elastic component of the free-energy, which takes into account the oriented hampering of the swelling-induced deformations due to the presence of stiffer

fibers. We also characterize the homogeneous free-swelling solutions of the corresponding anisotropic stress-diffusion problem; we present an asymptotic approximation of the key equations, which allows us to explicitly derive the anisotropic solution of the problem in terms of stretch $\lambda_{\parallel}$ along the fiber direction and stretch $\lambda_{\perp}$ in the orthogonal plane. Then, we discuss a constitutive identification of our fiber-reinforced homogeneous material defined by the extended Flory–Rehner thermodynamic model with the limit material corresponding to the assembly of narrow softer and stiffer strips, based on the experiments already presented in the literature.[6] Precisely, a relationship between the elastic moduli of the limit homogeneous material and those of the low-swelling and high-swelling gels is determined; with this, the analysis of systems based on assemblies of narrow strips of softer and stiffer gels, such as the bilayer systems discussed in the following sections, can be implemented.

Inspired by the plant world, where anisotropic swelling is realized in different systems through the coupling of cellulose fibrils and highly swellable matrix[9] and controlled *via* the orientation of the fibrils within the matrix, we analyze thin bilayered gel sheets where the layers have different anisotropic structures. We discuss the swelling-induced change of shape of pinecone-like sheets and seedpod-like sheets, corresponding to systems showing bending and twisting deformation modes, respectively.[10] In this last case, we observe a transition from helicoid-like shapes to ribbon-like shapes, depending on the aspect ratio of the bilayered sheet. This kind of behavior has been already observed in nature with reference to different physical situations,[10–12] and different modelings have been proposed, which neglect the elastic contribution of swelling-induced deformations. It is noteworthy that in our modeling helicoid-like and ribbon-like shapes come from the elastic deformation of composite sheets which, due to the anisotropic structure of their components, undergo anisotropic swelling.

[a] Sapienza Università di Roma, via Eudossiana 18, Roma, Italy. E-mail: paola.nardinocchi@uniroma1.it; Fax: +39 06 4884852; Tel: +39 06 44585242
[b] Università Roma Tre, via della Vasca Navale 84, Roma, Italy

2. The extended Flory–Rehner model

The Flory–Rehner model[13,14] for stress diffusion in gels is based on a representation form of the free energy $\phi(\mathbf{F}_d, c_d)$, which depends on the deformation gradient $\mathbf{F}_d$ from the initial dry configuration of the polymer gel, and on the molar solvent concentration c_d per unit dry volume. Precisely, it accounts additively for the elastic energy of the polymer network and for the polymer–solvent mixing energy:

$$\phi(\mathbf{F}_d, c_d) = \frac{1}{2} G(\mathbf{F}_d \cdot \mathbf{F}_d - 3) + \frac{RT}{\Omega} h(c_d), \qquad (2.1)$$

with

$$h(c_d) = \Omega c_d \ln\left(\frac{\Omega c_d}{1 + \Omega c_d}\right) + \chi(T) \frac{\Omega c_d}{1 + \Omega c_d}, \qquad (2.2)$$

with G being the shear modulus of the dry polymer, T the temperature, Ω the solvent molar volume, R the universal gas constant, and χ a dimensionless parameter, possibly depending on the temperature, which represents the dis-affinity between the polymer and the solvent, whose physical interpretation at the microscopic level relies on the lattice theory for polymer solutions, which relates χ to the free-energy excess due to the mixing of the solvent and the polymer.† Key features of ϕ are as follows: (i) ϕ is the density per unit volume of the dry polymer; (ii) the elastic contribution hampers swelling; (iii) the mixing contribution favors swelling. The molecular incompressibility hypothesis of both the polymer and the solvent implies that det $\mathbf{F}_d = 1 + \Omega c_d$, that is, changes in volume are only due to solvent absorption. The isotropic structure of ϕ determines locally isotropic swelling processes. In particular, under free conditions (unconstrained gels) swelling processes only involve a change in size, if homogeneous gels are considered.

We imagine to put reinforcements (fibers) into swellable polymer gels and create a composite whose shape changes can be programmed by adjusting the fiber orientation. To describe the equilibrium shapes of these gels, we propose a revised version of the Flory–Rehner free energy, which accounts for the anisotropic elasticity of the polymer network due to the stiff fibers that hamper swelling along their direction:

$$\phi^{\mathrm{ani}}(\mathbf{F}_d, c_d) = \phi(\mathbf{F}_d, c_d) + \frac{1}{2} G\gamma(\mathbf{F}_d\mathbf{e} \cdot \mathbf{F}_d\mathbf{e} - 1)^2, \qquad (2.3)$$

with γ as a stiffening parameter and the unit vector field $\mathbf{e}$ as the fiber direction. The idea of describing the effects of the elastic anisotropic response by adding energetic contributions based on some invariants of deformations, as the second summand in (2.3), was introduced in the early 90s[16] to describe the mechanical behavior of the anisotropic material, and the mechanical meaning of the parameter γ has been largely investigated through deformation tests.[17] Thenceforth, it has been largely adopted in the literature dealing with biological anisotropic materials, together with more complex constitutive

† The polymer–solvent dimensionless mixing energy is often represented by its density $h/(1 + \Omega c_d)$ per unit current volume of the polymer–solvent system (see ref. 15).

models, always based on the so-called structural models of the elastic energy.[18] The constitutive equations delivering both the reference stress $\mathbf{S}$ (aka first Piola–Kirchhoff stress) and the chemical potential μ come from thermodynamic issues and prescribe that

$$\mathbf{S} = G\mathbf{F}_d + 2G\gamma(\mathbf{F}_d\mathbf{e} \cdot \mathbf{F}_d\mathbf{e} - 1)\mathbf{F}_d\mathbf{e} \otimes \mathbf{e} - p\mathbf{F}_d^*, \qquad (2.4)$$

$$\mu = RT\left(\ln \frac{\Omega c_d}{1 + \Omega c_d} + \frac{1}{1 + \Omega c_d} + \frac{\chi}{(1 + \Omega c_d)^2}\right) + \Omega p,$$

where $\mathbf{F}_d^* = (\det \mathbf{F}_d)\mathbf{F}_d^{-T}$ and the indeterminate pressure field p can be interpreted as the reaction associated with the volumetric constraint.[19]

The unconstrained fibered gel immersed in a solvent bath of chemical potential μ_{ext} attains its equilibrium conditions when $\mathbf{S}$ satisfies the boundary conditions concerning the possible boundary tractions and μ is homogeneous within the gel and equal to μ_{ext}.

3. Anisotropic free-swelling solutions

We start by looking for homogeneous anisotropic swelling for a fibered parallelepiped by setting

$$\mathbf{F}_d = \lambda_\parallel \mathbf{e} \otimes \mathbf{e} + \lambda_\perp \check{\mathbf{I}} \text{ and } c_d = \frac{1}{\Omega}\left(\lambda_\parallel \lambda_\perp^2 - 1\right), \qquad (3.5)$$

with $\lambda_\parallel$ and $\lambda_\perp$ being the linear swelling ratio along the fiber direction and in the orthogonal plane, respectively, $J = \lambda_\parallel \lambda_\perp^2$ the swelling ratio, and $\check{\mathbf{I}} = \mathbf{I} - \mathbf{e} \otimes \mathbf{e}$. With this, eqn (2.4) deliver

$$S_\parallel = \mathbf{S}\mathbf{e} \cdot \mathbf{e} = G\lambda_\parallel + 2G\gamma(\lambda_\parallel^2 - 1)\lambda_\parallel - p\lambda_\perp^2, \qquad (3.6)$$

$$S_\perp = \mathbf{S} \cdot \check{\mathbf{I}} = G\lambda_\perp - p\lambda_\parallel \lambda_\perp, \qquad (3.7)$$

for the stress component along the fiber direction and in the orthogonal plane, respectively, and

$$\mu = RT\left(\ln \frac{\lambda_\parallel \lambda_\perp^2 - 1}{\lambda_\parallel \lambda_\perp^2} + \frac{1}{\lambda_\parallel \lambda_\perp^2} + \frac{\chi}{\left(\lambda_\parallel \lambda_\perp^2\right)^2}\right) + \Omega p, \qquad (3.8)$$

for the chemical potential. Homogeneous solutions $(\lambda_\parallel, \lambda_\perp, p)$ of the problem satisfy the following three equations

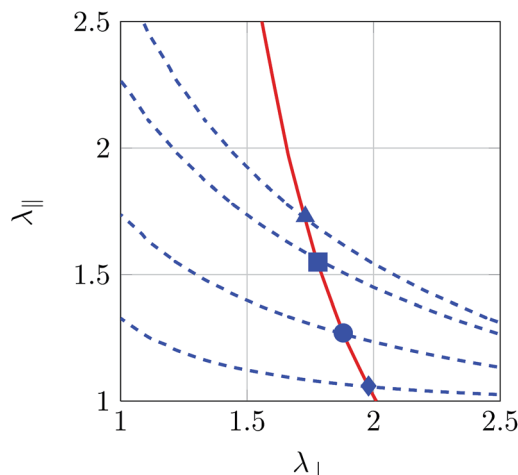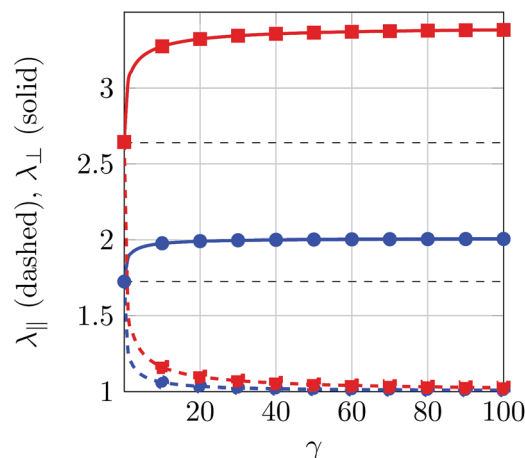$$S_\parallel = \check{S}_p(\lambda_\parallel, \lambda_\perp, p) = \sigma_\parallel, \qquad (3.9)$$

$$S_\perp = \check{S}_t(\lambda_\parallel, \lambda_\perp, p) = \sigma_\perp, \qquad (3.10)$$

$$\mu = \check{\mu}(\lambda_\parallel, \lambda_\perp, p) = \mu_{\mathrm{ext}}, \qquad (3.11)$$

where $\sigma_\parallel$ and $\sigma_\perp$ are the boundary tractions on the faces of unit normal $\mathbf{e}$, and on the other faces of the parallelepiped, respectively.

Once p is solved from eqn (3.11) and inserted into eqn (3.9) and (3.10), solutions $(\lambda_\parallel, \lambda_\perp)$ can be represented in the $\lambda_\parallel, \lambda_\perp$ plane as the intersection points of $\sigma_\parallel$ and $\sigma_\perp$ stress isolines. In particular, for $\sigma_\parallel = \sigma_\perp = 0$, free swelling anisotropic solutions are recovered and are shown in Fig. 1. Therein, we fix $G = 1$

Fig. 1 On the plane $(\lambda_\parallel, \lambda_\perp)$ we report the isoline $S_\perp = 0$ (solid, red) and the isolines $S_\parallel = 0$ (dashed, blue) for different values of γ. For a given γ, anisotropic free swelling is determined by the intersection point of the isolines $S_\perp = 0$ and $S_\parallel = 0$. The plot shows four of such points, corresponding to $\gamma = 0$, 0.1, 1, and 10 (triangle, square, circle, and diamond); the elastic modulus is $G = 1$ MPa.
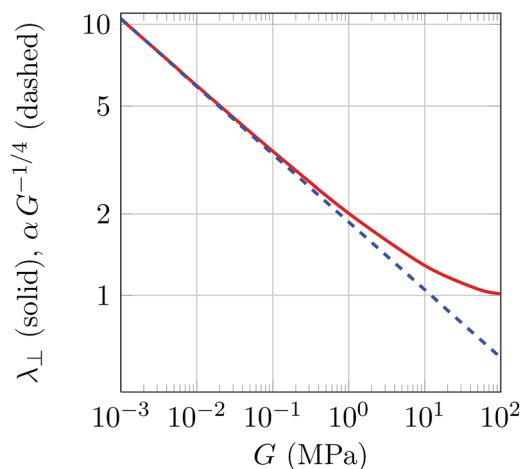

Fig. 2 Anisotropic enhancement: the anisotropic swelling increases with the parameter γ, and this effect is more pronounced for low values of the shear modulus G. Both $\lambda_\parallel$ and $\lambda_\perp$ approach very fast to their asymptotic values: $\lambda_\parallel \to 1$ for any G, while the asymptotic value of $\lambda_\perp$ depends on G. The plot shows $\lambda_\perp$ (solid), and $\lambda_\parallel$ (dashed) versus γ for $G = 1$ MPa (circles, blue), and $G = 0.1$ MPa (squares, red). The constant dashed-lines represent the isotropic solutions.

MPa, $\Omega = 6 \times 10^{-5}$ m^3 mol^{-1}, $\chi = 0.2$, $T = 293$ K, and $R = 8.31$ J mol^{-1} K^{-1}; moreover, we set $\mu_{ext} = 0$, and note that the stress component $S_\perp$ does not depend on the stiffening parameter γ (see the solid red line) whereas the isolines $S_\parallel = 0$ change with γ (see the dashed blue lines). We show the anisotropic solutions corresponding to four different values of γ, identified by triangle, square, circle, and diamond for $\gamma = 0$, 0.1, 1, and 10, respectively. In particular, for $\gamma = 0$, the free-swelling isotropic solution is recovered, that is, $\lambda_\parallel = \lambda_\perp$; by increasing γ, that is, the stiffness of the fibers, the swelling ratio $\lambda_\parallel$ decreases whereas the swelling ratio $\lambda_\perp$ increases, thus yielding an anisotropic deformation. It is worth noting that, in the framework of the Flory–Rehner theory, the chemical potential μ_{ext} of the solvent bath, together with the elastic properties of the material G and γ, determines the free swelling state at equilibrium, and thus, the value of the swelling ratio J; in particular, the lower the shear modulus G, the higher the swelling ratio J. The effect of the material parameter γ is that of hampering the strain along the fiber direction; thus, for $\gamma \to \infty$ the material becomes infinitely stiff along that direction, and $\lambda_\parallel \to 1$, for any G. Concurrently, the whole swelling is realised through an expansion in the plane orthogonal to the fiber direction, and $\lambda_\perp \to \sqrt{J}$. Fig. 2 shows how the anisotropic swelling increases with the parameter γ, and how this effect is more pronounced for low values of the shear modulus G: $\lambda_\parallel$ (dashed), and $\lambda_\perp$ (solid) are plotted against γ for $G = 1$ MPa (circles, blue), and $G = 0.1$ MPa (squares, red).

Following the asymptotic approximation already presented in ref. 8, eqn (3.6)–(3.8) and (3.9)–(3.11) may be rearranged to give

$$\frac{G\Omega}{RT} \simeq \left(\frac{1}{2} - \chi\right)\frac{\lambda_\parallel}{J^2} = \left(\frac{1}{2} - \chi\right)\lambda_\parallel^{-5}\left(1 + 2\gamma\left(\lambda_\parallel^2 - 1\right)\right)^{-2}, \quad (3.12)$$

up to $O(\lambda_\parallel^{-2}\lambda_\perp^{-6})$, when $\sigma_\parallel = \sigma_\perp = \mu_{ext} = 0$, and $G\Omega/RT = 1$. The equation is highly nonlinear in $\lambda_\parallel$, and cannot be solved explicitly; however, the asymptotic behavior of the ratios $\lambda_\parallel$ and $\lambda_\perp$ when $\gamma \to \infty$ may be derived. As $J = \lambda_\parallel\lambda_\perp^2 > 0$, we conclude that $\lambda_\parallel > 0$. Therefore, there must exist a lower bound for $\lambda_\parallel$ as γ increases, that is $d\lambda_\parallel/d\gamma = 0$ as $\gamma \to \infty$. Then, deriving eqn (3.12) with respect to γ and setting $d\lambda_\parallel/d\gamma = 0$ yields $\lambda_\parallel \to 1$. Moreover, as $J = \lambda_\parallel\lambda_\perp^2$, we conclude $\lambda_\perp \to \sqrt{J}$. Finally, when $\lambda_\parallel = 1$, eqn (3.12) yields

$$\lim_{\gamma \to \infty} \lambda_\perp = \alpha G^{-1/4}, \alpha = \left(\frac{(1/2 - \chi)RT}{\Omega}\right)^{1/4}. \quad (3.13)$$

The comparison between this explicit estimate and the numerical solution is shown in Fig. 3: the agreement is excellent as long as $G\Omega/RT \ll 1$.

Fig. 3 Asymptotic values of $\lambda_\perp$ versus shear modulus G (red, solid), compared with its explicit estimate $\lambda_\perp = \alpha G^{-1/4}$ (blue, dashed).

3.1 The limit material

Recently, the swelling of photo-crosslinkable hydrogel sheets, patterned with alternating parallel strips of the material with high and low equilibrium extents of swelling was discussed; these sheets are manufactured through a programmed variation of the degree of crosslinking, realized by changing the dose of UV light. It was shown that those photo-patterned sheets deform by rolling around the axis perpendicular to the interface between high- and low-swelling regions; in particular, when the strip width falls below a critical size proportional to the film thickness, the patterned sheets instead remain flat, undergoing anisotropic swelling.[6] In this limit, the material can be homogenized and described by our revised Flory–Rehner free energy assuming the director field **e** to be parallel to the longitudinal axis of the strips.

We discuss through a simple three-step constitutive identification model, based on the work presented in ref. 6, the relationship between the elastic constants (G, γ) of the anisotropic material presented in the previous section and the elastic moduli of the materials in the high- and low-swelling regions (Fig. 4 shows a cartoon of the three-step procedure: 1, 2, and 3). The first step (1) consists of the assumption that the high and low swelling gel materials, when swollen separately, follow the standard Flory–Rehner model; λ_h and λ_l are the swelling ratios, respectively. Hence, the ratio of the corresponding shear moduli is determined as

$$\frac{G_h}{G_l} \simeq \left(\frac{\lambda_h}{\lambda_l}\right)^{-5}. \qquad (3.14)$$

The second step (2) consists of using the relationships experimentally determined in ref. 6 between the ratio λ_h/λ_l and the anisotropic swelling ratios $\lambda_\parallel$ and $\lambda_\perp$ (see Fig. (9)$_B$ in ref. 6). The third step (3) consists of assembling our eqn (3.9)–(3.11) to get
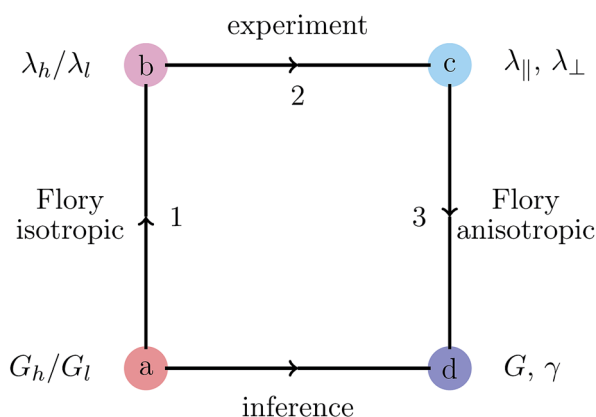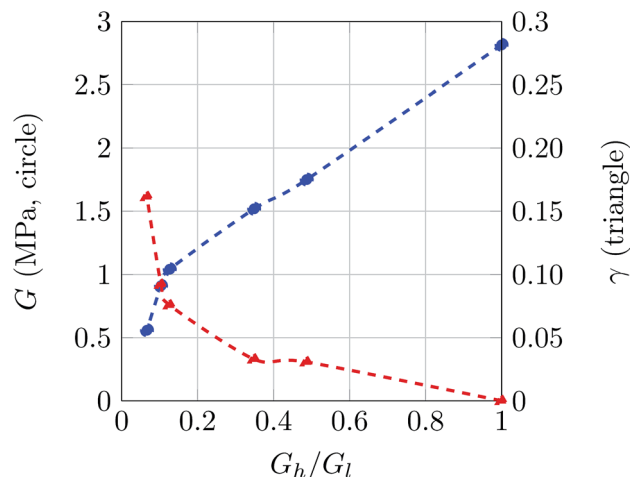

Fig. 5 Shear modulus G (circle, blue) and stiffening parameter γ (triangle, red) of the homogeneous limit material *versus* the ratio G_h/G_l of the shear moduli of the high-swelling and low-swelling gels.

$$\lambda_\perp^2 = (1 + 2\gamma(\lambda_\parallel^2 - 1))\lambda_\parallel^2, \qquad (3.15)$$

$$G\Omega\frac{1}{\lambda_\parallel} = -RT\left(\ln\frac{\lambda_\parallel\lambda_\perp^2 - 1}{\lambda_\parallel\lambda_\perp^2} + \frac{1}{\lambda_\parallel\lambda_\perp^2} + \frac{\chi}{\left(\lambda_\parallel\lambda_\perp^2\right)^2}\right),$$

where we assumed $\sigma_\parallel = \sigma_\perp = 0$, and in deriving the pair (G, γ) corresponding to the pair $(\lambda_\parallel, \lambda_\perp)$. The three steps allow us to identify a relationship between the ratio G_h/G_l and the pair (G, γ), and is shown in Fig. 5. Given the elastic moduli of the softer and stiffer strips, the pair (G, γ) of the homogeneous fibered material corresponding to the assembly with very narrow strips can be determined. We observe that for $G_h/G_l = 1$, that is for a homogeneous (and isotropic) material, we get $\gamma = 0$ and $G \simeq 2.9$ MPa, in good agreement with the value $G = G_l \simeq 2.98$ MPa determined from the asymptotic approximation prescribed by the Flory model when $\lambda_l^2 = 2.1$ as in ref. 6.

4. Bilayered anisotropic systems

In the plant world, anisotropic swelling is realized through the coupling of cellulose fibrils and highly swellable matrix[9] and controlled *via* the orientation of the fibrils within the matrix, so realizing different deformation modes. In ref. 10, the plant cell wall architecture was divided into two categories according to bending or twisting deformation modes of the corresponding seed dispersal units, described as follows. The pinecone scale is an elongated, bilayer structure, comprised roughly of a lower section with strong reinforcement consisting of stiff cellulose microfibrils perpendicular to the long axis of the scale, and an upper section with reinforcement along the long axis of the scale, see cartoon in Fig. 6(a). Upon drying, these cell walls show an anisotropic shrinkage with minor deformation in the axial direction on the upper side and in the direction orthogonal to the cell axis on the lower side; the combined action on the two layers leads to a bending of the scale, which opens the cone.[9,20]

Fig. 4 Inference of the relation $G_h/G_l \to (G, \gamma)$. The path from (a) to (d) is the following: given the ratio G_h/G_l, the Flory model for isotropic gels yields the ratio λ_h/λ_l; the experiment in ref. 6 yields the map $\lambda_h/\lambda_l \to (\lambda_\parallel, \lambda_\perp)$; finally, the extended Flory model for anisotropic gels furnishes the final step $(\lambda_\parallel, \lambda_\perp) \to (G, \gamma)$.
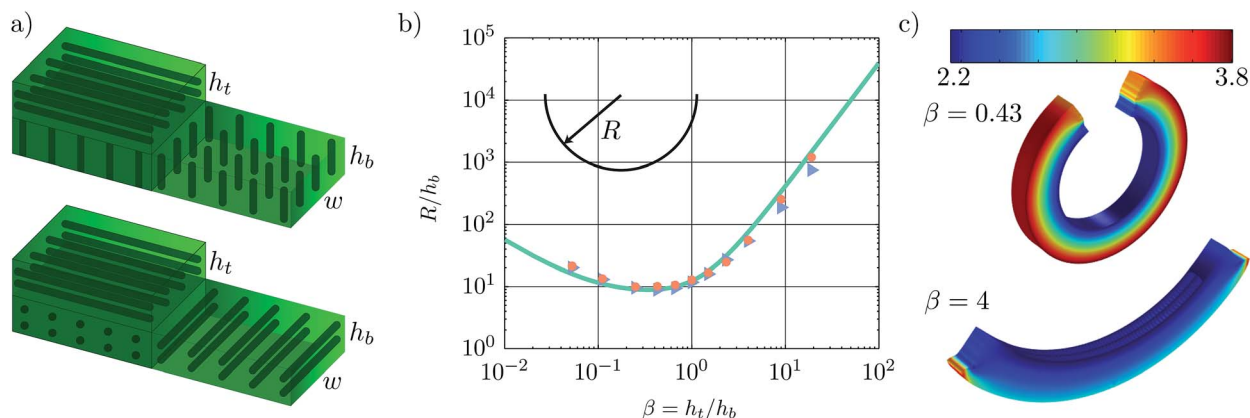
Fig. 6 Bending modes: (a) schematic of the fiber orientation (pinecone-like, top; plane crossed bilayer, bottom); (b) dimensionless radius of curvature *versus* β at $\mu_{ext} = 0$: from finite element simulations for pinecone-like sheets (circles) and for plane crossed bilayers (triangles); the outcomes of the 1D analytical model (solid line) are the same for both the fiber orientation considered; (c) deformed shapes of the pinecone-like sheets got from finite element simulation for $\beta = 0.43$ and $\beta = 4$: the color code describes the longitudinal stretch.

Likewise, orchid tree seedpods present the inner layer of the pod valve made of fiber cells oriented roughly at 45° to the pod axis and the outer layer made of elongated cells oriented perpendicularly to the inner fiber cells. When drying, the seedpod of orchid tree opens with its two halves twisting helically away from each other.[10]

Inspired by these natural systems, we discuss the deformation modes of thin bilayered and swellable structures, when fibers are differently oriented in the two homogeneous fibered layers. Different three-dimensional configurations can be realized, depending on the orientation of the stiffer fibers in the two layers of the structure; here, we only present and discuss the transition from flat to curved shapes suffered by pinecone-like and seedpod-like sheets under free swelling conditions.

Given a bilayer sheet, we fix a cartesian orthonormal basis ($\mathbf{e}_1$, $\mathbf{e}_2$, and $\mathbf{e}_3$) such that the unit vector $\mathbf{e}_1$ spans the longitudinal axis of the sheet and $\mathbf{e}_3$ identifies the unit normal $\mathbf{m}$ to the mid surface of the sheet; the corresponding coordinate system is denoted as x_1, x_2, and x_3. The thicknesses of the top and bottom layers are h_t and h_b, respectively; w, L, and $h = h_t + h_b$ are the width, length, and the total thickness of the sheet.

4.1 Pinecone-like sheets

The anisotropic structure of the two layers in pinecone-like thin sheets is shown in Fig. 6 (panel a, top). Stiffer fibers are aligned to the longitudinal axis of the sheet in the top layer whereas are orthogonal to the sheet mid surface in the bottom layer, that is, $\mathbf{e} \equiv \mathbf{e}_1$ and $\mathbf{e} \equiv \mathbf{e}_3$ in the top and bottom layers, respectively. As it is well known, the ratios h_t/h_b and G_t/G_b of thicknesses and shear moduli are key parameters for the mechanical behavior of the composite sheet.[21,22] In a swelling-induced bending, also the longitudinal swelling ratio mismatch $\lambda_{ot} - \lambda_{ob}$ has a decisive role in determining the amount of bending, with λ_{ot} and λ_{ob} being the longitudinal swelling ratio that the top and bottom layers would have separately, which are determined in this case by[8]

$$\lambda_{ot} = \lambda_{\parallel} \text{ and } \lambda_{ob} = \lambda_{\perp}. \tag{4.16}$$

We assume $G_t = G_b = G$ and $\gamma_t = \gamma_b = \gamma$, that is, the two layers differ from each other only due to the orientation of the fibers. Moreover, we assume that the swelling ratio orthogonal to the sheet of the longitudinal axis does not contribute to bending. With this, and with reference to the structural model presented and discussed in ref. 8, we set

$$\lambda(x_3) = \Lambda_o(1 + x_3 \Lambda_o \kappa) \tag{4.17}$$

for the longitudinal stretch suffered by the composite sheet during bending with uniform axis stretch Λ_o and axis curvature κ; and

$$\sigma_t(x_3) = 3G(\lambda(x_3)/\lambda_{\parallel} - 1), \ \sigma_b(x_3) = 3G(\lambda(x_3)/\lambda_{\perp} - 1), \tag{4.18}$$

for the longitudinal stresses on the top and bottom layers, respectively. In absence of any forces and torques, the total longitudinal force and the total torque on the sheet have to be identically null:

$$w \int_{-\frac{h}{2}}^{h(\beta)} \sigma_b(x_3)dx_3 + w \int_{h(\beta)}^{\frac{h}{2}} \sigma_t(x_3)dx_3 = 0, \tag{4.19}$$

$$w \int_{-\frac{h}{2}}^{h(\beta)} x_3 \sigma_b(x_3)dx_3 + w \int_{h(\beta)}^{\frac{h}{2}} x_3 \sigma_t(x_3)dx_3 = 0,$$

with $\beta = h_t/h_b$ and $h(\beta) = h/2 - \beta h/(1 + \beta)$. Eqn (4.19) deliver the following linear system of two equations in Λ_0 and $\Lambda_1 = \kappa \Lambda_0{}^2$:

$$\left(\frac{A_t}{\lambda_{\parallel}} + \frac{A_b}{\lambda_{\perp}}\right)\Lambda_0 + \left(\frac{S_t}{\lambda_{\parallel}} + \frac{S_b}{\lambda_{\perp}}\right)\Lambda_1 = A, \ A = A_t + A_b,$$

$$\left(\frac{S_t}{\lambda_{\parallel}} + \frac{S_b}{\lambda_{\perp}}\right)\Lambda_0 + \left(\frac{I_t}{\lambda_{\parallel}} + \frac{I_b}{\lambda_{\perp}}\right)\Lambda_1 = 0, \tag{4.20}$$

with A_t, S_t, and I_t being the area, the static moment and the moment of inertia with respect to the coordinate axis spanned by e_2 of the cross-section of the top layer; A_b, S_b, and I_b have an analogous meaning for the bottom layer. The swelling ratios $\lambda_\parallel$ and $\lambda_\perp$ are known numerically for each layer once G and γ are given (see Fig. 2); however, when $\gamma \to \infty$ we have shown that they may be computed explicitly. Hence, the curvature of the sheet may be easily evaluated as a function of β, once fixed the elastic and geometrical characteristics of the two layers. The solid line in Fig. 6 (panel b) represents the dimensionless radius of curvature R/h_b versus β, with $R = 1/\kappa$, when $G = 40$ kPa, $\gamma = 0.1$, $\Omega = 6 \times 10^{-5}$ m^3 mol^{-1}, $T = 293$ K, and $h = 1$ mm, $w = 0.4$ mm, and $L = 8$ mm.

We also propose a set of numerical experiments, based on the nonlinear three-dimensional stress-diffusion model proposed in the previous section. We only study the equilibrium configurations attained by the bilayered structure when it is embedded into a solvent bath of assigned chemical potential, through the computational model presented in ref. 19, appropriately revised to take into account the anisotropic thermodynamic model. We solve the numerical problem for different values of β. The outcomes of the numerical simulations are represented in Fig. 6 (panel b) through circles, together with the analytical results represented by the solid line, and shows a uniform curvature of the pinecone-like sheet. We also note that in our numerical experiments we use continuous displacement fields; thus, the discontinuity in the longitudinal stress across the interface between the two layers is smeared through a boundary layer whose size is very small with respect the thickness of the sheet. In the end, Fig. 6 (panel c) shows the curved three-dimensional configurations assumed by the composite sheet when the bottom layer is almost twice the top layer ($\beta = 0.43$) and when the bottom layer is very thin ($\beta = 4$).

It is worth noting that, for a different anisotropic structure within the bottom layer such that $e \equiv e_3$ (denoted as plane crossed bilayer), see Fig. 6 (panel a, bottom), the three-dimensional changes of shape of the composite remains almost unchanged with respect to the pinecone situation. As expected, the radius of curvature versus β pattern is unmodified by the different fiber orientations in the bottom layer whereas the outcomes of the numerical experiments (triangles) almost overlap the ones of pinecone-like sheets, as Fig. 6 (panel b) shows.

It means that the bending behavior observed in both bilayered structures depends on the presence of stiff reinforcements on the top layer along the longitudinal axis. The mismatch between the longitudinal deformations within the two layers determines the bent configuration as the minimal energy configuration. At the end, the bent configuration allows maximum expansion for the bottom region along the longitudinal axis (which always remains in the transverse isotropy plane for both bilayered structures), while minimizing longitudinal deformation in the top region.

4.2 Seedpod-like sheets

The anisotropic feature of seedpod-like sheets is shown in Fig. 7 (panel a). Fibers are oriented at $\pm 45°$ with respect to the longitudinal axis e_1 of the sheet in the two layers: $e = \cos 45° e_1 + \sin 45° e_2$ and $e = \cos 45° e_1 - \sin 45° e_2$ within the top and bottom layer, respectively. In this case, what is expected is a twisting behavior; indeed, the two layers of seedpod-like sheet present reinforcements perpendicular to one at each other; it means that the maximum expansion for the two layers occurs at orthogonal directions and, as none of them comprises the longitudinal axis of the sheet, twisting is generated.

We follow ref. 11, and start with a qualitative analysis. We consider the top and bottom layers of thickness $h_t = h_b = h/2$ anisotropically swollen with parallel and transverse free-swelling stretches $\lambda_\parallel$ and $\lambda_\perp$, along the fiber direction and in the orthogonal direction, respectively. We imagine that a homogeneous swelling-induced deformation $\mathbf{F}_o = \lambda_\parallel e \otimes e + \lambda_\perp \check{\mathbf{I}}$ can be realized within each layer via embedding in a solvent bath, if each layer was free from the rest of the system. Due to the different anisotropic structures, the bottom layer swell at an
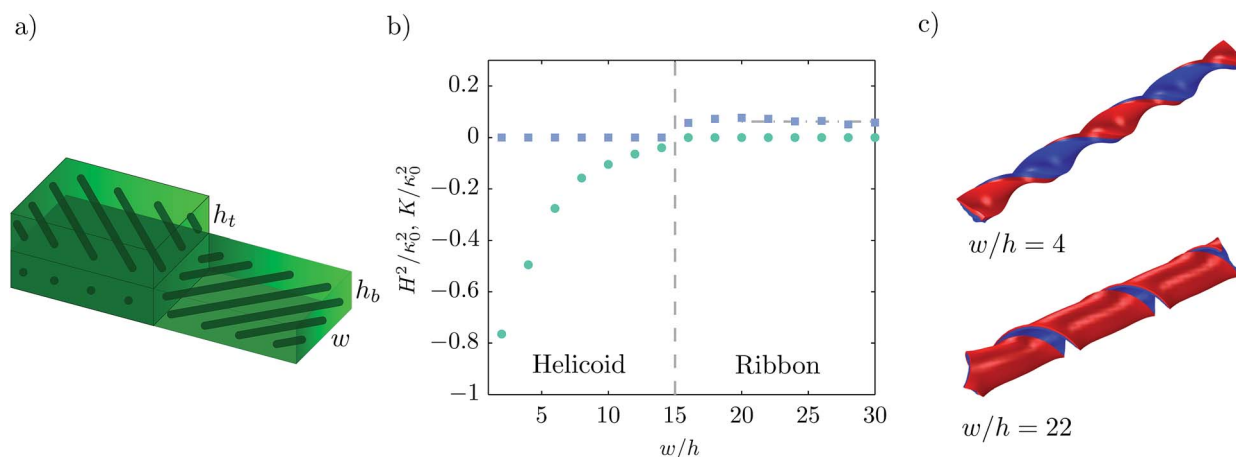

Fig. 7 Twisting modes: (a) schematics of the fiber orientation; (b) $H^2/\kappa_o^2 - w/h$ (squares) and $K/\kappa_o^2 - w/h$ (circles) patterns at equilibrium for $\mu_{ext} = 0$, at the center of the mid-surface; (c) helicoid-like and ribbon-like three-dimensional configurations corresponding to small and large aspect ratios, respectively.

angle of 90° with respect to the top layer and the corresponding three-dimensional metrics $g_o^{(t)}$ and $g_o^{(b)}$ would be different and given by:

$$g_o^{(t)} = \begin{pmatrix} \frac{1}{2}\left(\lambda_p{}^2 + \lambda_t{}^2\right) & \frac{1}{2}\left(\lambda_t{}^2 - \lambda_p{}^2\right) & 0 \\ . & \frac{1}{2}\left(\lambda_p{}^2 + \lambda_t{}^2\right) & 0 \\ 0 & 0 & \lambda_t{}^2 \end{pmatrix}, \quad (4.21)$$

and

$$g_o^{(b)} = \begin{pmatrix} \frac{1}{2}\left(\lambda_p{}^2 + \lambda_t{}^2\right) & -\frac{1}{2}\left(\lambda_t{}^2 - \lambda_p{}^2\right) & 0 \\ . & \frac{1}{2}\left(\lambda_p{}^2 + \lambda_t{}^2\right) & 0 \\ 0 & 0 & \lambda_t{}^2 \end{pmatrix}, \quad (4.22)$$

with $(g_o^{(t)})_{ij} = (\mathbf{F}_o{}^T \mathbf{F}_o)\mathbf{e}_j \cdot \mathbf{e}_i$ and $\mathbf{F}_o$ being the swelling-induced deformation of the top layer (the same arguments hold for the bottom layer). We now imagine that the two swollen layers are glued on top of the other; the composite sheet is so incompatible. Following ref. 11, we approximate the resulting three-dimensional metric g_o of the composite sheet by the linear approximation $g_o = (g_o^{(t)} + g_o^{(b)})/2 + x_3/h(g_o^{(t)} - g_o^{(b)})$ and view the thin sheet as a shell with the first and second natural fundamental forms given by

$$a_o(x_1, x_2) = g_o(x_1, x_2, 0) = \frac{1}{2}\left(\lambda_\parallel{}^2 + \lambda_\perp{}^2\right)\begin{pmatrix} 1 & 0 \\ 0 & 1 \end{pmatrix} \quad (4.23)$$

and

$$b_o(x_1, x_2) = -\frac{1}{2}\frac{\partial g_o}{\partial x_3}(x_1, x_2, 0) = -\frac{1}{2h}\left(\lambda_\parallel{}^2 - \lambda_\perp{}^2\right)\begin{pmatrix} 0 & 1 \\ 1 & 0 \end{pmatrix}. \quad (4.24)$$

Rescaling the lengths by $((\lambda_\parallel{}^2 + \lambda_\perp{}^2)/2)^{1/2}$, we get the rescaled first and second fundamental form as

$$\bar{a}_o(x_1, x_2) = \begin{pmatrix} 1 & 0 \\ 0 & 1 \end{pmatrix} \text{ and } \bar{b}_o(x_1, x_2) = \begin{pmatrix} 0 & \kappa_o \\ \kappa_o & 0 \end{pmatrix}, \quad (4.25)$$

with $\kappa_o = (1/h)(\lambda_\perp{}^2 - \lambda_\parallel{}^2)/(\lambda_\perp{}^2 + \lambda_\parallel{}^2)$. Neglecting the elastic contribution of the fibers, the (dimensionless) elastic energy of such a shell is

$$\mathscr{E} = \int_0^L \int_{-w/2}^{w/2} \left((1-\nu)|a - a_o|^2 + \nu tr^2(a - a_o)\right) dx_1, dx_2 + \frac{h^2}{3}\int_0^L \int_{-w/2}^{w/2}\left((1-\nu)|b - b_o|^2 + \nu tr^2(b - b_o)\right) dx_1, dx_2,$$

with a and b being the first and second fundamental forms of the realized surface; the first row describes the stretching contribution whereas the second row the bending contribution. The competition between the stretching-dominated regime ($a = a_o$) and bending-dominated regime ($b = b_o$) determines the realization of ribbon and helicoids, respectively. In ref. 11 it was shown that the critical aspect ratio w/h determining the threshold between a stretching-dominated and a bending-dominated regime is equal to $1/\sqrt{\kappa_o h}$. In ref. 11, κ_o must be

measured experimentally; we can determine it analytically by taking advantage of the 1D model for pinecones. Indeed, as the model describes a 1D planar Kirchhoff beam without external forces, the natural curvature is completely realized and it is therefore equal to κ. We therefore cut the seedpod-like sheets at 45° so as to get the beam represented in Fig. 6 (a, bottom). In this way, the natural curvature κ_o that cannot be realized in 2D geometry turns out to be the curvature attained by the beam. Precisely, for $\mu_{ext}/\mu_o = 0$, $G = 40$ kPa, $\gamma = 0.1$, and $\beta = 1$, we got $\kappa_o = 160$ m^{-1}.

We planned a set of numerical experiments, based on the nonlinear three-dimensional stress-diffusion model proposed in the previous section, to quantitatively investigate the dependence of the three-dimensional final shape of the composite sheet both on the aspect ratio and on the chemical potential of the external bath. Firstly, we fixed $\mu_{ext} = 0$ J mol^{-1}, and studied the change of shape obtained at equilibrium by the composite sheet for different aspect ratios w/h. We evaluated the Gaussian curvature K and the square of the mean curvature H^2 over the mid surface of the sheet. We computed $K = \kappa_1 \kappa_2$ and $H = (\kappa_1 + \kappa_2)/2$, respectively, with κ_1 and κ_2 as the principal curvatures of the mid-surface of the sheet obtained by the diagonalization of the second fundamental form $b_\alpha{}^\beta = a^{\beta\eta}b_{\eta\alpha}$ (actually realized) of the middle surface with $a_{\beta\eta} = \mathbf{a}_\beta \cdot \mathbf{a}_\eta$, $a^{\beta\eta} = (a_{\beta\eta})^{-1}$ and $b_{\eta\alpha} = \mathbf{n} \cdot \mathbf{a}_{\eta,\alpha}$ (greek indices may be equal to 1 or 2) and

$$\mathbf{n} = \frac{\mathbf{a}_1 \times \mathbf{a}_2}{|\mathbf{a}_1 \times \mathbf{a}_2|} \text{ and } \mathbf{a}_\alpha(x_1, x_2) = \mathbf{F}_d(x_1, x_2, 0)\mathbf{e}_\alpha. \quad (4.26)$$

We found that both K and H are uniform fields for ribbons ($K = 0$) whereas $H = 0$ and $K \propto -x_2{}^{-4}$ for helicoids. We represented them through the dimensionless curvatures $K/\kappa_o{}^2$ (circles) and $H^2/\kappa_o{}^2$ (squares) for different aspect ratios in Fig. 7, where the helicoid-ribbon transition can be appreciated. The transition occurs around $w/h = 15$; the same figure (panel c) shows two configurations obtained for $w/h = 4$ and $w/h = 22$. It is worth noting that the mean curvature exhibits an upper boundary for very large aspect ratios, $H^2/\kappa_o{}^2 \simeq 1/16$.

In ref. 11, the mean curvature for a very large aspect ratio was estimated as $H = (1 - \nu)\kappa_o/2$; as the numerical experiments allow us to determine the relationship between H and μ_{ext}, we determine κ_o as a function of μ_{ext} by setting $\nu = 1/2$ and using the fact that $H = (1 - \nu)\kappa_o/2$. When $\mu_{ext} = 0$, the natural curvature κ_o is found to be equal to 160 m^{-1}. This value is of the same order of magnitude of the ones presented in ref. 11 and is equal to the one we measured by means of the beam model.

Finally, Fig. 8 shows the pattern of the dimensionless principal curvatures κ_1/κ_o and κ_2/κ_o (evaluated in the center of the mid-surface) for different dimensionless chemical potentials μ_{ext}/μ_o of the solvent bath, for $w/h = 4$ (helicoid, solid red) and $w/h = 22$ (ribbon, dashed green). Note how the transition of helicoid to ribbon occurs smoothly as the chemical potential increases: when $w/h = 22$, the two principal curvatures start to deviate from zero in a symmetric way (helicoid) but when $\mu_{ext}/\mu_o \simeq -0.1$, one of them starts decreasing up to zero (ribbon). This smooth transition may be explained by remembering that the
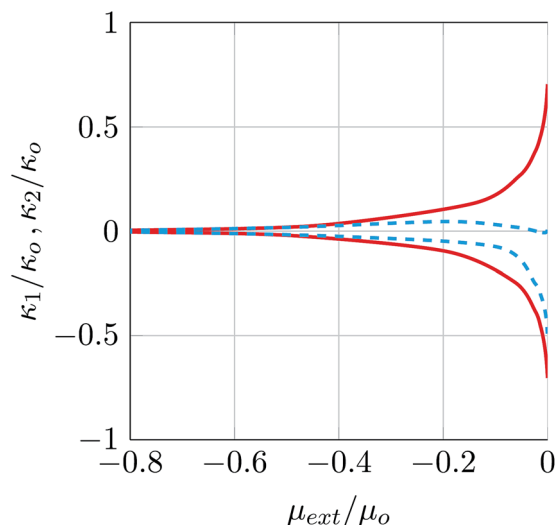
Fig. 8 Dimensionless principal curvatures for helicoids (solid, red) and ribbons (dashed, green) *versus* dimensionless chemical potential of the external bath. The aspect ratios are $w/h = 4$ for the helicoid and $w/h = 22$ for the ribbon.

critical aspect ratio w/h is equal to $1/\sqrt{\kappa_o h}$ that, as we have just shown, is a function of the chemical potential μ_{ext}.

5. Conclusions

In conclusion, we described the anisotropic swelling within the Flory–Rehner thermodynamic model through an extension of the elastic component of the free-energy, which takes into account the oriented hampering of the swelling-induced deformations due to the presence of stiffer fibers. We also characterized the homogeneous free-swelling solutions of the corresponding anisotropic stress-diffusion problem; we presented an asymptotic approximation of the key equations which allows us to explicitly derive the anisotropic solution of the problem. We also proposed an identification of the constitutive procedure aimed to characterize both the Young's modulus and the stiffening parameter in terms of the elastic and swelling characteristics of micropatterned (hard/soft) gel sheets. Actually, the problem of identifying those parameters in terms of the microstructure of the sheets remains unsolved; appropriate tests should be done before swelling, along the road map successfully followed within the field of biological tissues with a directional microstructure.[17,18]

We discussed the swelling-induced change of shape of pinecone-like strips and seedpod-like strips, corresponding to systems showing bending and twisting deformation modes, respectively. In this last case, we observe a transition from helicoid-like shapes to ribbon-like shapes, depending on the aspect ratio of the bilayered sheet. This kind of behavior has been already observed in nature with reference to different physical situations,[10–12,23] and different modelings have been proposed which neglect the elastic contribution of swelling-

induced deformations. It is noteworthy that in our modeling helicoid-like and ribbon-like shapes come from the elastic deformation of the composite sheet which, due to the anisotropic structure of its components, undergoes anisotropic swelling.

Acknowledgements

References

1 S. Dai, P. Ravi and K. C. Tam, *Soft Matter*, 2009, **5**, 2513–2533.
2 T. Wallmersperger, K. Keller, B. Krplin, M. Gnther and G. Gerlach, *Colloid Polym. Sci.*, 2011, **289**, 535–544.
3 J. Kim, J. A. Hanna, R. C. Hayward and C. D. Santangelo, *Soft Matter*, 2012, **8**, 2375–2381.
4 P. Nardinocchi and M. Pezzulla, *J. Appl. Phys.*, 2013, **113**, 22906.
5 J. Kim, J. A. Hanna, M. Byun, C. D. Santangelo and R. C. Hayward, *Science*, 2012, **335**, 1201–1205.
6 M. Byun, C. D. Santangelo and R. C. Hayward, *Soft Matter*, 2013, **9**, 8264–8273.
7 Z. L. Wu, M. Moshe, J. Greener, H. Therien-Aubin, Z. Nie, E. Sharon and E. Kumacheva, *Nat. Commun.*, 2013, **4**, 1586.
8 A. Lucantonio, P. Nardinocchi and M. Pezzulla, *Philos. Trans. R. Soc., A*, 2014, **470**, 20140467.
9 I. Burgert and P. Fratzl, *Philos. Trans. R. Soc., A*, 2009, **367**, 1541–1557.
10 R. M. Erb, J. S. Sander, R. Grisch and A. Studart, *Nat. Commun.*, 2013, **4**, 1712.
11 S. Armon, E. Efrati, R. Kupferman and E. Sharon, *Science*, 2011, **333**, 1726–1730.
12 L. Teresi and V. Varano, *Soft Matter*, 2013, **9**, 3081–3088.
13 P. J. Flory and J. Rehner, *J. Chem. Phys.*, 1943, **11**, 512–520.
14 P. J. Flory and J. Rehner, *J. Chem. Phys.*, 1943, **11**, 521–526.
15 M. Doi, *J. Phys. Soc. Jpn.*, 2009, **78**, 052001.
16 A. J. Spencer, *Continuum Theory of the Mechanics of Fibre-Reinforced Composites*, Springer-Verlag, 1984.
17 J. Merodio and R. W. Ogden, *Int. J. Non. Lin. Mech.*, 2005, **40**, 213–227.
18 J. D. Humphrey, *Cardiovascular Solid Mechanics: Cells, Tissues, and Organs*, Springer-Verlag, New York, 2002.
19 A. Lucantonio, P. Nardinocchi and L. Teresi, *J. Mech. Phys. Solids*, 2013, **61**, 205–218.
20 C. Dawson, J. F. V. Vincent and A. M. Rocca, *Nature*, 1997, **390**, 668.
21 S. Timoshenko, *J. Opt. Soc. Am. Rev. Sci. Instrum.*, 1925, **11**, 233–255.
22 B. A. Boley and J. H. Weiner, *Theory of Thermal Stresses*, Dover, 1997.
23 S. Armon, H. Aharoni, M. Moshe and E. Sharon, *Soft Matter*, 2014, **10**, 2733–2740.